Mapping the Human Cortical Surface by Combining Quantitative T_1 with Retinotopy[†]

Martin I. Sereno[1,3], Antoine Lutti[2], Nikolaus Weiskopf[2,] and Frederic Dick[3]

[1]Cognitive Perceptual and Brain Sciences, [2]Wellcome Trust Centre for Neuroimaging, UCL Institute of Neurology, University College London, London, UK and [3]Department of Psychological Sciences, Birkbeck/UCL Centre for NeuroImaging (BUCNI), Birkbeck College, University of London, London, UK

Address correspondence to Martin I. Sereno, Birkbeck/UCL Centre for NeuroImaging, 26 Bedford Way, London WC1H 0AP, UK. Email: m.sereno@ucl.ac.uk

We combined quantitative relaxation rate ($R_1 = 1/T_1$) mapping—to measure local myelination—with fMRI-based retinotopy. Gray–white and pial surfaces were reconstructed and used to sample R_1 at different cortical depths. Like myelination, R_1 decreased from deeper to superficial layers. R_1 decreased passing from V1 and MT, to immediately surrounding areas, then to the angular gyrus. High R_1 was correlated across the cortex with convex local curvature so the data was first "de-curved". By overlaying R_1 and retinotopic maps, we found that many visual area borders were associated with significant R_1 increases including V1, V3A, MT, V6, V6A, V8/VO1, FST, and VIP. Surprisingly, retinotopic MT occupied only the posterior portion of an oval-shaped lateral occipital R_1 maximum. R_1 maps were reproducible within individuals and comparable between subjects without intensity normalization, enabling multi-center studies of development, aging, and disease progression, and structure/function mapping in other modalities.

Keywords: MT, myelination, parcellation, surface reconstruction, visual areas

Introduction

Cortical areas are best defined and recognized on the basis of multiple converging techniques (Allman and Kaas 1971). Five measures developed during invasive experiments on animals include 1) receptotopic organization (e.g. retinotopy), 2) architectonic features, 3) connection patterns, 4) neurophysiological properties, and 5) effects of localized lesions. These measures have each been adapted to human brains. Studies on the effects of brain damage in humans have a long pedigree, recently supplemented by transcranial magnetic stimulation studies in normal subjects. Cortical-surface-based functional magnetic resonance imaging retinotopy (Engel et al. 1994; Sereno et al. 1995; DeYoe et al. 1996) is now established and often combined with functional studies, which constitute the overwhelming majority of in vivo human neuroimaging experiments. Connection patterns are beginning to be addressed in vivo with diffusion-imaging-based fiber-tracking methods. But despite the historical precedence of postmortem human architectonic studies, in vivo human architectonics has perhaps been the least well-adapted of the 5 measures.

Postmortem cortical parcellation remains an difficult problem a century after the publication of Brodmann's classic cytoarchitectonic maps of the cortex in humans and other species. Related early work using cytoarchitectonic and myeloarchitectonic methods soon resulted in a plethora of human cortical area maps (reviews: Zilles and Amunts 2010; Geyer et al. 2011). But human cortical parcellation then went into decline, especially after the blistering critique of Lashley and Clark (1946). Bailey and von Bonin (1951), for example, divided the human neocortex into only 6 areas, even blurring the sharp border between V1 and V2 originally recognized by Meynert (1867).

Despite subsequent advances in mapping cortical areas in non-human primates (Merzenich and Kaas 1980), specifically human cortical parcellation languished (though see Braak (1980) on "pigmento"-architectonics). The growth of human neuroimaging in the 1980s had the effect of elevating Brodmann's map—after a rough translation from Brodmann's 2D summary images to a 3D atlas—to a world standard. Despite its acknowledged shortcomings (e.g. the middle temporal area (MT/V5) did not appear), the moderate resolution of early volume-averaged neuroimaging data did not initially demand better. Two decades later, as modern postmortem human cortical architectonics augmented by immunohistochemistry began to appear, the situation has improved considerably (e.g. Malikovic et al. 2007; Caspers et al. 2012).

However, a persistent stumbling block to combining structural and functional data has been to integrate postmortem parcellations based on high-resolution microscopic measures with retinotopic, connectional, and functional data from in vivo brains. Variability between postmortem and in vivo brains—whether at the single subject or group level—introduces irreducible uncontrolled systematic variation.

Most previous attempts at in vivo architectonics have only been able to consider few localized regions of the cortex (Clark et al. 1992; Walters et al. 2003; Eickhoff et al. 2005; Sigalovsky et al. 2006; Geyer et al. 2011). One reason is signal-to-noise constraints due to in vivo scan time limits. But a more serious problem is the difficulty of reliably detecting small signal differences (1–4%) between different parts of non-quantitative T_1-weighted (T_1w) images that have large artifactual variations in brightness and contrast due to uncorrected inhomogeneities in the local radiofrequency transmit and receive fields. Widely applied post hoc histogram-based normalization methods (e.g. Dale et al. 1999) and T_1w/T_2 weighted (T_2w) ratio methods (Glasser and Van Essen 2011) remain sensitive to the effects of uncorrected B1 "transmit" inhomogeneities (flip-angle variation) on brightness and contrast, which affect both within- and between-individual comparisons. Ratio methods must also contend with vessel artifacts and local spatial distortion that differ between the 2 scan types, and unfavorable error propagation inherent in
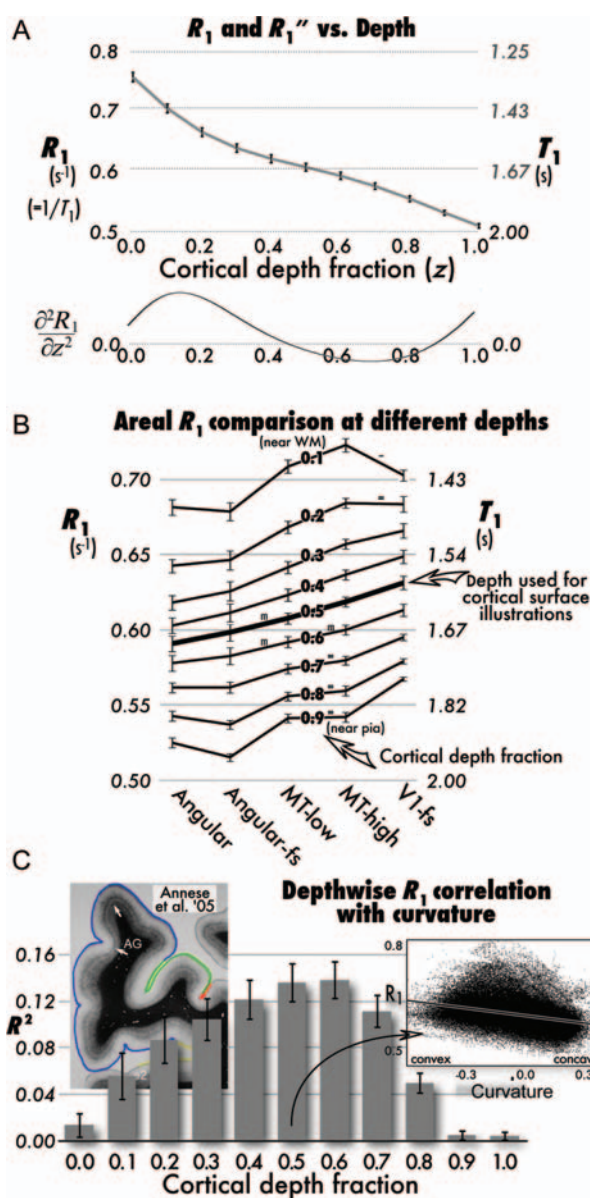
Figure 1. Relaxation rate (R_1) as function of cortical depth, area, and curvature. (A) Overall cortical average R_1 (equivalent T_1 on right y-axis) decreases monotonically from gray–white boundary (depth fraction 0.0) to a slight plateau at middle depths (0.3–0.6, beginning where second derivative in lower graph crosses zero), and then resumes its decrease in superficial layers (0.7–1.0; error bars: ±1 standard error of the mean over subjects). (B) Cross-ROI differences in average cortical R_1 shown as line for 8 depths (from 0.1 near white matter to 0.9 near pia); y-axes, error bars as in (A); ROIs: Angular (angular gyrus), angular-fs (FreeSurfer angular gyrus label), MT low and MT high [non-overlapping low- and high-probability MT labels (Malikovic et al. 2007; Fischl et al. 2008), V1-fs (FreeSurfer V1)]. All matched-paired *t*-tests on hypothesized differences significant ($P < 0.05$) except where marked "m" ($P < 0.1$), "=" (no significant difference), or "-" (difference opposite prediction). (C) Vertex-wise correlation (adjusted R^2) of R_1 and curvature as function of depth (error bars as before over subjects). Scatter plot inset at right is from a single subject at depth 0.5. For comparison, left inset shows myelin-stained section of human cortex with reduced myelination in concave areas (compare 2 white arrows, from Annese et al. 2004).

ratio estimation. Finally, differences in local cortical curvature (convex vs. concave) systematically affect the laminar and myeloarchitecture of the cortex, even within a cortical area (Fig. 1; Smart and McSherry 1986; Annese et al. 2004).

Here, we present a detailed analysis that combines functional and structural data. To overcome the inherent limitations of non-quantitative structural imaging listed above, quantitative T_1 maps were acquired for all subjects, providing a measure of local myeloarchitecture (Schmierer et al. 2004; Draganski et al. 2011). The quantification allows for the direct comparison of datasets acquired on different subjects at different times and different MRI sites. The T_1 maps were then combined with retinotopic mapping across multiple sessions in the same group of subjects. High-resolution cortical-surface reconstructions of the gray–white matter and pial surfaces were made from the structural scans and used to analyze, visualize, and fuse the T_1 and retinotopy data. Since the longitudinal relaxation rate, $R_1 (=1/T_1)$, positively correlates with the level of myelination and the brightness of T_1w scans as commonly used for morphometry, we henceforth refer exclusively to it.

Materials and Methods

Six subjects (ages 22–55, 3 female) with normal or corrected-to-normal vision participated in all parts of the study. Experimental protocols were approved by local ethics committees, and participants gave informed and signed written consent.
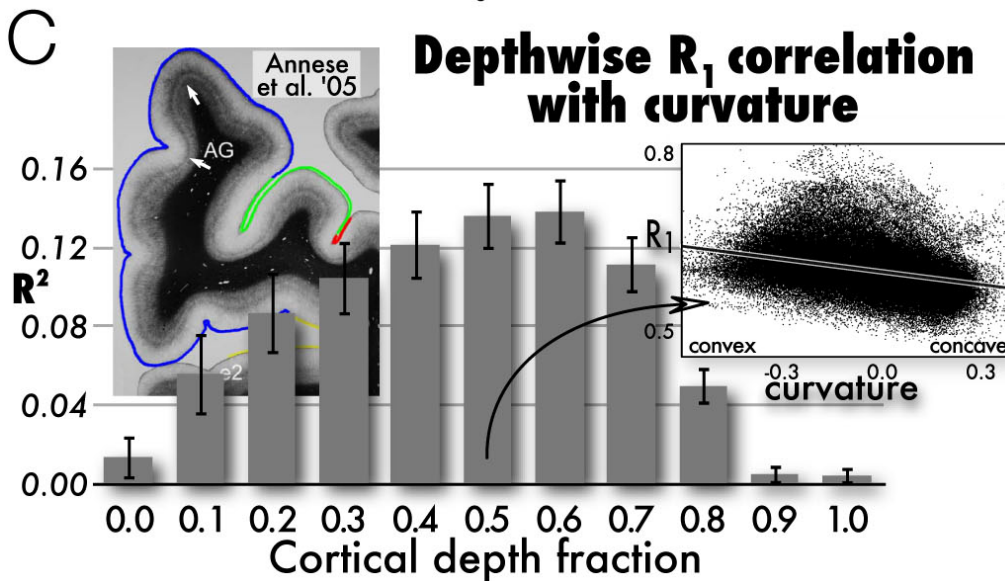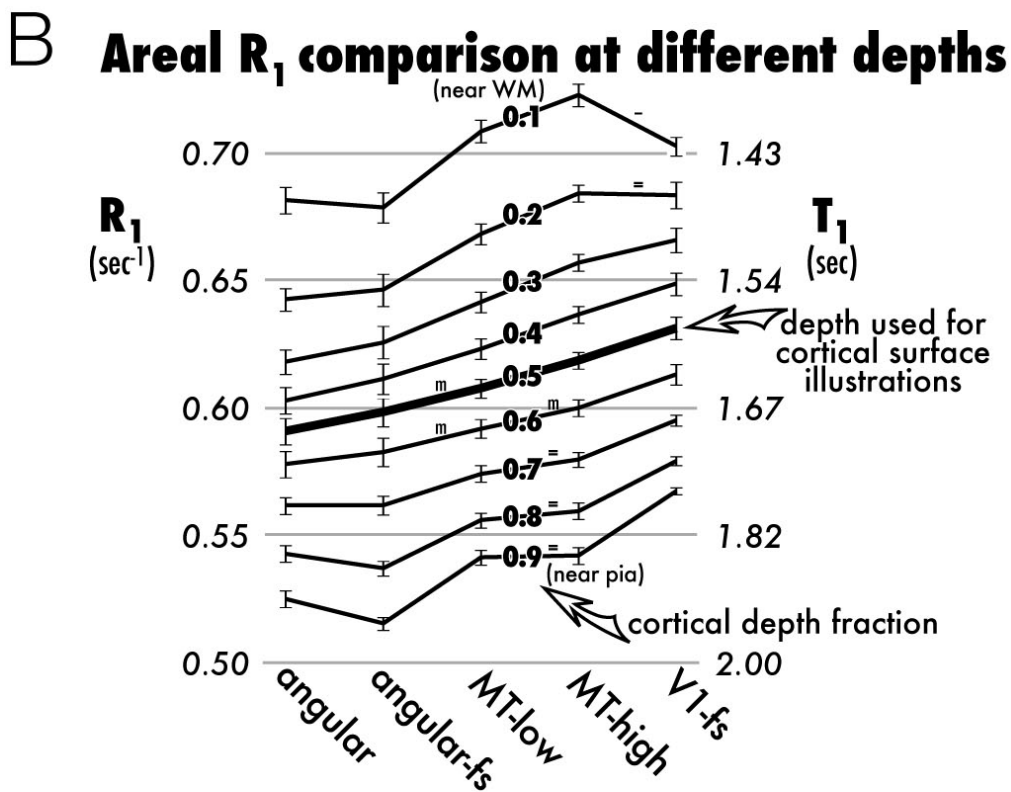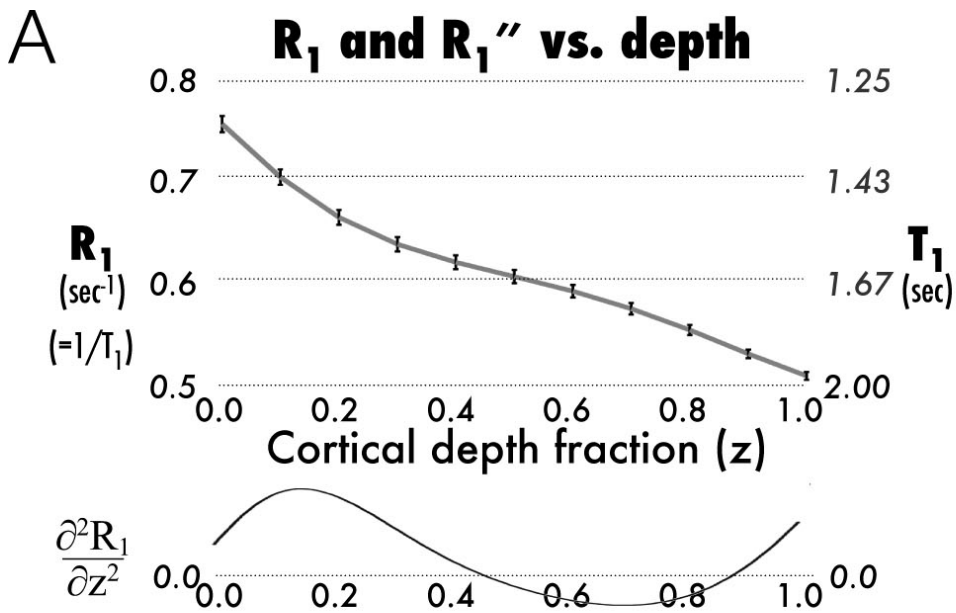
Structural Imaging

Structural images were acquired on a whole-body Tim Trio system (nominal field strength 3T, actual 2.89T, Siemens Healthcare, Erlangen, Germany), with body transmit and 32-channel receive head coil at the Wellcome Trust Centre for Neuroimaging. Proton density-weighted (PDw) and T_1w images were acquired using an in-house multi-echo 3D FLASH pulse sequence (Weiskopf et al. 2011; voxel size: $0.8 \times 0.8 \times 0.81$ mm³, field of view (FOV) = $256 \times 216 \times 194$ mm, matrix = $320 \times 270 \times 240$, repetition time (TR) = 23.7 ms, excitation flip angle: 6° (PDw) or 28° (T_1w)). Acquisition was speeded up by 2× GRAPPA parallel imaging in the phase encoding and 6/8 Partial Fourier in the partition direction. To improve image quality, 4 gradient echoes were acquired (echo delay times (TE) = 2.2, 4.75, 7.3, 9.85 ms) after each excitation pulse. Each session consisted of four 10 min 31 s acquisitions (2 PDw and 2 T_1w) and 2 shorter scans to estimate field inhomogeneities (see below). Quantitative R_1 maps were estimated from the PDw and T_1w images according to the formalism developed by Helms et al. (2008) including a correction for imperfect RF spoiling (Preibisch and Deichmann 2009). Recent applications of this method have demonstrated its robustness (Helms et al. 2008, 2009; Draganski et al. 2011). To correct for the effect of radio frequency (RF) transmit inhomogeneities on R_1 maps, maps of the transmit field B1$^+$ were acquired using a 3D echo-planar imaging (EPI) spin-echo (SE)/stimulated echo (STE) method (Lutti et al. 2010, 2012; FOV = $256 \times 192 \times 192$ mm³, matrix = $64 \times 48 \times 48$, TE$_{SE}$/TE$_{STE}$ = 39.38/72.62 ms, TR = 500 ms, acquisition time 3 min 48 s), which was corrected for off-resonance effects using a B0 fieldmap. For further details, see Supplementary Information.

Functional Imaging and Analysis

Standard T_2*-weighted EPI scans (3.2-mm isotropic resolution, 128 or 256 volumes each) and a T_1w alignment scan with the same orientation and slice block center were acquired on a 1.5 whole-body Tim Avanto system (Siemens Healthcare) at the Birkbeck/UCL Centre for NeuroImaging, with body transmit and 32-channel receive head coil (see Supplementary Information for details). Five of 6 subjects completed at least 8 retinotopy scans (4 scans in 1 subject) and 4 ipsilateral mapping scans (2560 volumes per subject) across 3–5 additional sessions. See Supplementary Information for details of surface-based retinotopy analysis.

In-house OpenGL/Xlib software drove a video front-projection direct-view system that stimulated the visual field to an eccentricity of at least 57° of visual angle in all directions from central fixation. Balanced (clockwise/counterclockwise, in/out) phase-encoded polar

A   R₁ and R₁″ vs. depth

A — R_1 and R_1'' vs. depth

R_1 (sec^{-1}) (=1/T$_1$) axis: 0.8, 0.7, 0.6, 0.5

T_1 (sec) axis: 1.25, 1.43, 1.67, 2.00

Cortical depth fraction (z): 0.0, 0.2, 0.4, 0.6, 0.8, 1.0

$\dfrac{\partial^2 R_1}{\partial z^2}$ 0.0   0.0

B   Areal R₁ comparison at different depths

R_1 (sec^{-1}) axis: 0.70, 0.65, 0.60, 0.55, 0.50

T_1 (sec) axis: 1.43, 1.54, 1.67, 1.82, 2.00

Depth fractions: 0.1 (near WM), 0.2, 0.3, 0.4, 0.5, 0.6, 0.7, 0.8, 0.9 (near pia)

depth used for cortical surface illustrations

cortical depth fraction

x-axis: angular, angular-fs, MT-low, MT-high, V1-fs

C   Depthwise R₁ correlation with curvature

Annese et al. '05

AG

R^2 axis: 0.16, 0.12, 0.08, 0.04, 0.00

Cortical depth fraction: 0.0, 0.1, 0.2, 0.3, 0.4, 0.5, 0.6, 0.7, 0.8, 0.9, 1.0

Inset: R_1 axis 0.8, 0.5; convex, concave; curvature −0.3, 0.0, 0.3

angle (wedge) and eccentricity (ring) stimuli contained medium-luminance-contrast colored checkerboards, optical flow fields, and simultaneous monitor-for-upside-face-among-right-side-up and monitor-for-number-among-letters tasks to maintain continuous peripheral attention (eight 64 second cycles). Ipsilateral field mapping stimuli used low contrast moving versus stationary gratings avoiding the center-of-gaze and the vertical meridian (see Supplementary Information for details).

Cortical-Surface Reconstruction and Sampling of R_1 Values Within Cortical Ribbon

Cortical surfaces were reconstructed with FreeSurfer (v5.0.0) from the aligned (AFNI 3dAllineate, hand-inspected) average of the 2 high-resolution T_1w scans. We initially used quantitative R_1 scans but experienced localized segmentation failures because some boundaries between the pial surface, the CSF, and the skull have different contrast than what is currently assumed by FreeSurfer algorithms (see Discussion).

R_1 data sets were sampled along the normal to each gray–white matter surface vertex in steps of 10% of cortical thickness (thickness estimated in FreeSurfer; Fischl and Dale 2000) and then smoothed tangentially at each depth with a 4-mm full width half maximum (FWHM) 2D kernel. The FreeSurfer estimate of local curvature (smoothed with a 1-mm FWHM 2D kernel) was used as a linear predictor of R_1 values at each depth. Vertex-wise residuals from this regression were used as "de-curved" estimates of R_1 values whose units are directly comparable to raw de-meaned R_1 values. See Supplementary Information for details of R_1 region of interest (ROI) choice.

Results

R_1 as a Function of Cortical Depth

Postmortem studies of cortical myelination demonstrated a consistent pattern of myelination versus depth across most cortical areas. Myelination is highest immediately above the white matter, there are 2 bands of high myelination in deeper layers (inner/deeper and outer/shallower stria of Baillarger), and finally, there is a stepwise reduction in myelination in superficial layers. To investigate whether this overall pattern was apparent in our R_1 data, we sampled the R_1 values for each surface vertex at different fractional cortical depths, and then averaged these profiles across all vertices.

Average R_1 values (Fig. 1A) show an extremely consistent decrease from deep to superficial layers (small to large depth fractions, z). A moderate plateau in deeper cortical layers begins around depth fraction 0.3, where the second spatial derivative with respect to z ($\partial^2 R_1/\partial z^2$), shown immediately below, crosses zero (an inflection point). The pattern of R_1 with depth closely resembles the overall profile of myelination seen in postmortem histology. It is considerably smoother, not distinguishing the 2 stria of Baillarger, which is a reflection of much coarser sampling units of in vivo human MRI (0.8 mm^3 here) compared with histology (~0.01 mm^3), as well as the averaging of R_1 across the entire cortex of both hemispheres.

R_1 Variation over Probabilistically Defined Cortical ROIs

For an initial verification of regional differences in R_1 as a measure of myelination, we defined 5 ROIs with large expected myelination differences. The first was the FreeSurfer probabilistic V1 label (V1-fs). The second and third were MT high and MT low (non-overlapping high and low probability

of cross-subject overlap regions). Finally, we included 2 angular gyrus labels—a smaller one, angular, defined on our subjects (non-visually responsive region just superior to MT) and a larger one, angular-fs, from the FreeSurfer parcellation.

Based on the histological literature, we predicted 1) that R_1 in V1 and the MT ROIs should exceed R_1 in the angular gyrus ROIs at all cortical depths, and that V1 should have the highest R_1, 2) R_1 in high-probability MT should exceed R_1 in surrounding lower probability MT in deeper cortical layers (depth fractions 0.1–0.6). The systematic R_1 curves across areas at different depths illustrated in Figure 1B confirmed these predictions. All matched-paired t-tests were significant at $P < 0.05$ except where noted, with "m" indicating marginal (0.05 < P < 0.10) differences, "=" indicating no significant difference, and "-" indicating difference opposite to predicted direction. ROI-based analyses showed that at the level of macroscopic landmarks, our quantitative estimate of R_1 parallels known regional differences in myelination.

Relationship of R_1 to Local Cortical Curvature

The human cortex has deep sulci, but also a complex pattern of concavity and convexity, including many convex regions buried within major sulci. Postmortem studies in humans show that myeloarchitecture varies significantly with local cortical convexity (Annese et al. 2004); more convex regions are thicker and more myelinated, especially in middle and upper layers. We therefore examined the relationship between R_1 and local curvature as a function of cortical depth. Figure 1C shows that there is a moderately strong correlation between local curvature and R_1 at middle cortical depth fractions (up to a maximum average adjusted $R^2 = 0.14$) that falls off as one approaches the white matter and the pial surface. The bottom right inset scatterplot includes a least-squares fit line for R_1 against vertex-wise curvature; vertices in convex regions of the cortex (often but not exclusively on gyri) have higher R_1 than vertices in more concave regions. Since R_1 varies more at the gray–white matter border and at the pial border than it does within the cortex itself, small errors in tissue segmentation during surface reconstruction can have a large effect on laminar R_1 estimates near those boundaries. The fact that R_1/curvature correlation is strongest at middle sampling depths suggests that segmentation errors are not responsible for our result.

Because local curvature is also related to local cortical thickness (average vertex-wise adjusted correlation between curvature and thickness: Adjusted $R^2 = 0.081$), local cortical thickness might explain some of the variation in R_1. However, the strong correlation between convexity and R_1 survives the addition of vertex-wise thickness as a covariate. To minimize the effects of local curvature in our subsequent analyses of R_1 variation across the cortical sheet, we therefore initially regressed R_1 against curvature, and then used the "de-curved" residual values as our estimates of regional differences in cortical myelination.

Test–Retest Consistency of R_1 Across the Cortex

The top 3 rows of Figure 2 show medial and lateral views of the cortical-surface-based cross-subject average (Fischl et al. 1999) of R_1 from 6 subjects (2 R_1 scans each), displayed on 1 of the 6 subjects' surfaces. The top row (gray–white matter surface), second row (pial surface), and third through sixth
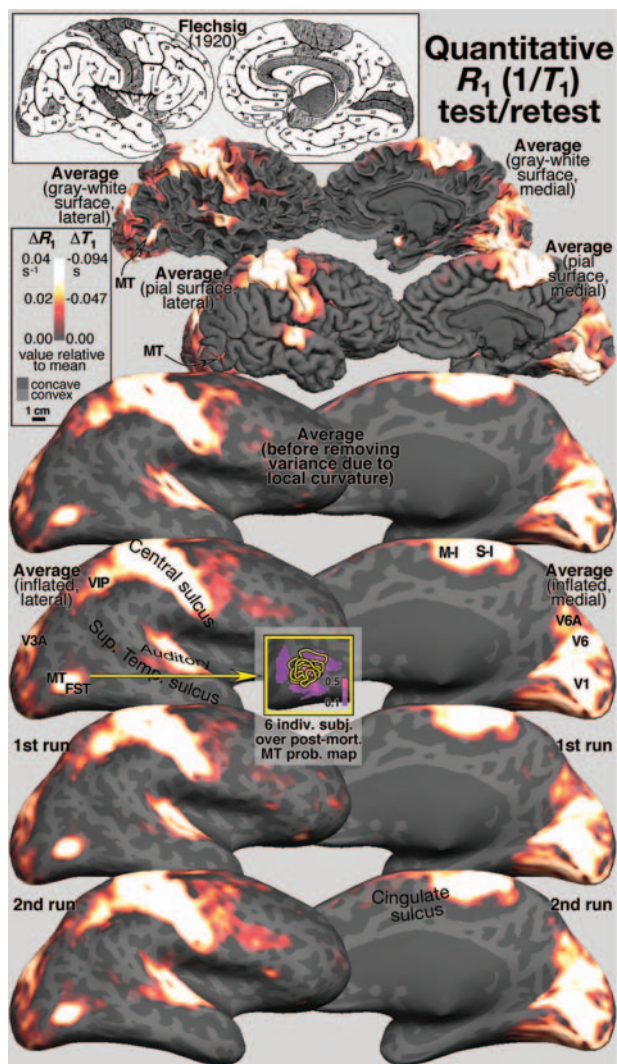
Figure 2. Cross-subject surface average relaxation rate (R_1) test/retest. Top left inset redrawn from Flechsig (1920) shows early myelinating areas in gray. Rows 1–6 show spherical morph cross-subject average ΔR_1 (difference above mean) projected back onto the gray–white, pial, and inflated surfaces of 1 subject. R_1 values in each subject were sampled at a point halfway between the individual's gray–white matter and pial surfaces. Row 3 shows the data before removing variance due to local cortical curvature; that variance is removed in all other rows. Rows 5 and 6 show excellent scan/rescan reliability of average. Lower middle inset shows same magnification lateral occipital cutout with individual subjects' R_1 maxima (yellow contours), superimposed on MT postmortem probability map in purple (Malikovic et al. 2007; Fischl et al. 2008), showing that the individual and average R_1 maxima differ subtly from the postmortem map. See text for midline and anterior insula mask.

rows (inflated surface) show same magnification views of one hemisphere. The heat scale overlay in all rows but row 3 shows "de-curved" R_1 values sampled from voxels lying at a cortical depth fraction of 0.5, while row 3 is not "de-curved" (but still de-meaned). The effects of "de-curving" can be seen by comparing rows 3 and 4 (e.g. the thin line posterior to MT disappears). Though regional variations in R_1 are small ($<0.04\,\text{s}^{-1}$), they are remarkably consistent over repeated measurements (bottom 2 rows). R_1 data were masked on the midline and in the anterior insula—in the first case because single hemisphere surfaces cut into the corpus callosum and thalamus, and in second case because of the difficulty of

accurately reconstructing the gray–white matter surface superficial to the claustrum. Small regions of high cortical R_1 in posterior cingulate and anterior insula may thus have been omitted here.

These data show a strong resemblance to Flechsig's (Flechsig 1920) survey of perinatal infant myelogenesis, re-rendered in the top left inset of Figure 2. Flechsig found that early myelinating cortical regions (dark shading) tended to be the most densely stained for myelin in the adult cortex. These regions are clearly visible in our R_1 data and include primary motor (M-I) and somatosensory (S-I) areas, primary and secondary auditory areas, as well as a number of visual areas described in more detail in the next section.
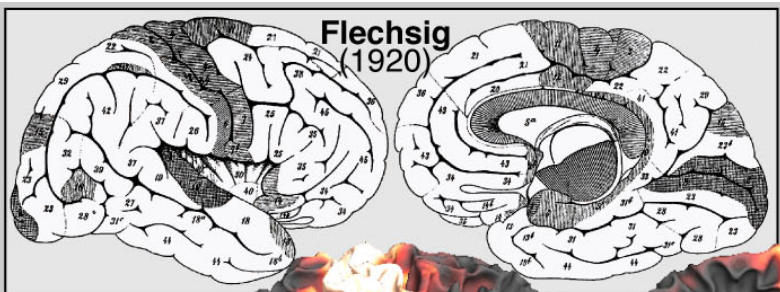
Relation of R_1 to Retinotopic Maps

Visual areas were mapped in the same set of 6 subjects using a wide-field direct-view front-projection system. In 2–3 additional scan sessions for each subject, we mapped polar angle, eccentricity, and ipsilateral low-contrast visual field representations (Huk et al. 2002). We then performed cortical-surface-based cross-subject averages of complex-valued (amplitude and phase) data (Sereno and Huang 2006; Hagler et al. 2007) and calculated visual field sign from the polar angle and eccentricity averages to identify borders in early areas (Sereno et al. 1995). A detailed pattern of correspondences between R_1 and retinotopic borders emerged when the 2 data sets were fused on the same surface.
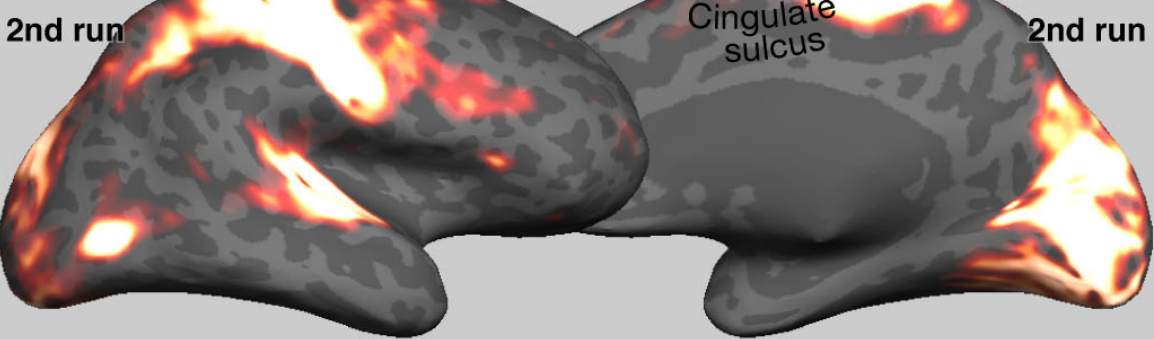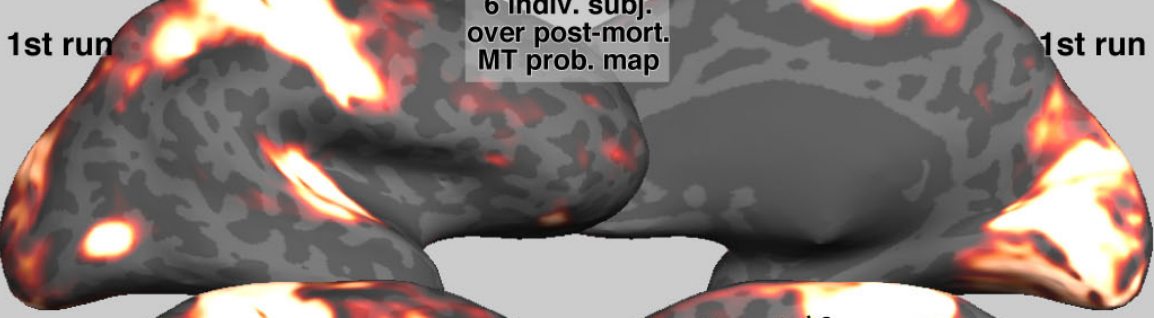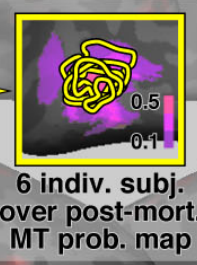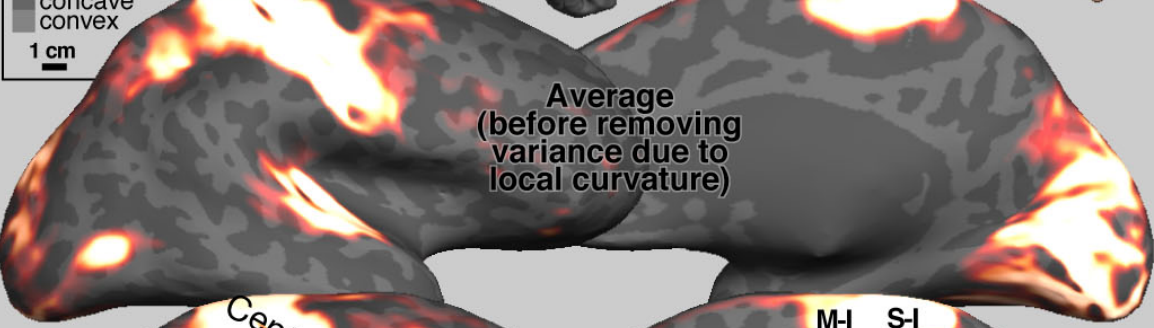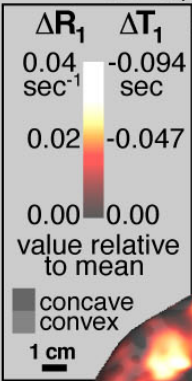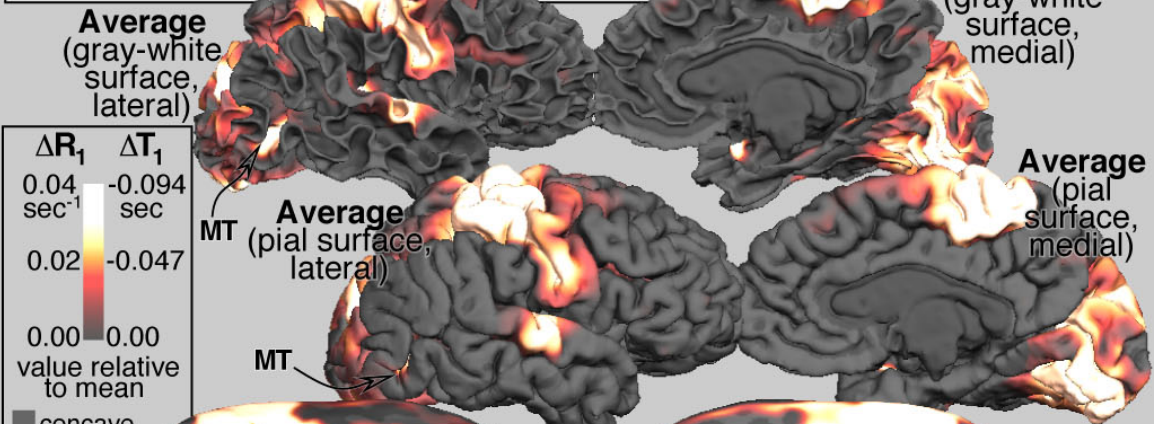
The retinotopic and R_1 averages from both hemispheres in Figures 3 and 4 are illustrated in identical lateral, posterior, medial, and inferior poses (inflated surface) to aid comparison and are described together. Iso-R_1 borders ($\Delta R_1 = 0.020\,\text{s}^{-1}$) around R_1 maxima were traced and superimposed on the polar angle data using thin white dashes to aid comparisons (see Supplementary Information for a movie that smoothly varies view and color scale contrast, more clearly illustrating the systematic fine level differences in the data shown in Fig. 4). Retinotopic borders (vertical meridian → circles, horizontal meridian → thick black dashes) are illustrated on both figures as is the posterior boundary of ipsilateral responses to low contrast moving gratings (thick yellow dashes in top row).

V1 (see medial views) was characterized by high R_1 (ΔR_1 ~$0.031\,\text{s}^{-1}$), and its retinotopically defined borders in both hemispheres corresponded almost exactly with a sharp drop in R_1. Superior to V1, V6 was bilaterally identified by a characteristic upper-to-lower field transition (moving superiorly and posteriorly) on the posterior bank of the parieto-occipital sulcus (Pitzalis et al. 2006) with R_1 values similar to V1 (ΔR_1 ~$0.035\,\text{s}^{-1}$) with a shallow R_1 valley between it and V1 (see contrast ramp movie in Supplementary Information). Interestingly, Flechsig (1920) identified an early myelinating medial area in an almost identical location (Fig. 2, top inset, medial view). There was an additional shallower maximum of myelination (ΔR_1 ~$0.012\,\text{s}^{-1}$) just anterior and superior to V6, containing mostly lower visual fields that we have tentatively labeled V6A (see Gamberini et al. 2011, for finer subdivisions).

In lateral occipital cortex, there was a prominent oval of high R_1 (ΔR_1 ~$0.029\,\text{s}^{-1}$). We initially expected this might correspond to MT/V5. However, both polar angle retinotopy (reversal at an upper visual field vertical meridian) and the posterior bound of ipsilateral responses were situated near

Quantitative R₁ (1/T₁) test/retest

Flechsig (1920)

Average (gray-white surface, lateral)

Average (gray-white surface, medial)

Average (pial surface, lateral)

Average (pial surface, medial)

MT

ΔR_1	ΔT_1
0.04 sec⁻¹	-0.094 sec
0.02	-0.047
0.00	0.00

value relative to mean

concave
convex

1 cm

Average (before removing variance due to local curvature)

Average (inflated, lateral)

VIP
Central sulcus
V3A
Sup. Temp. sulcus
Auditory
MT
FST

M-I   S-I

Average (inflated, medial)

V6A
V6
V1

6 indiv. subj. over post-mort. MT prob. map

0.5
0.1

1st run

1st run
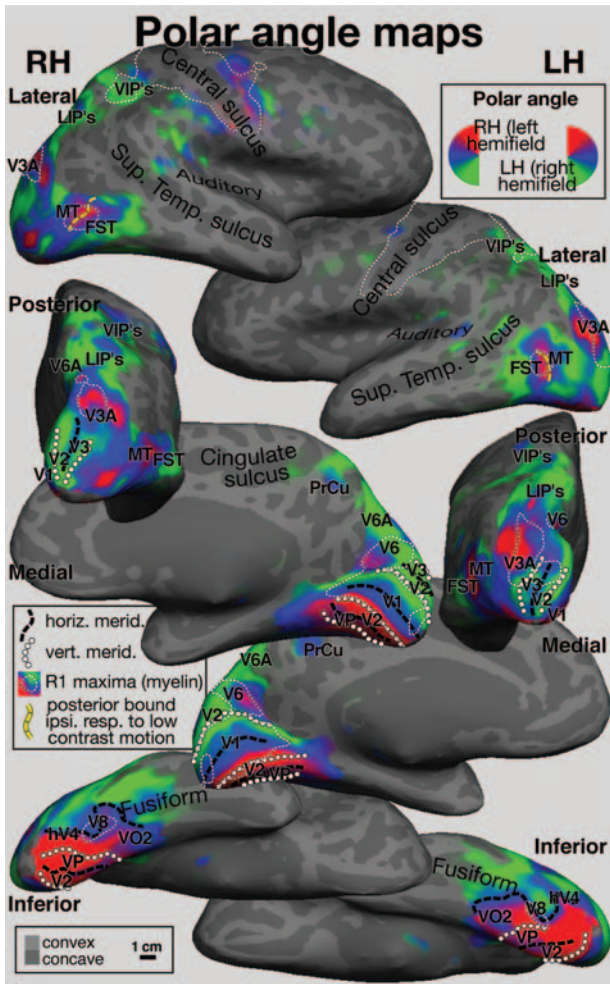
2nd run

Cingulate sulcus

2nd run

Figure 3. Cross-subject surface average retinotopic maps. Spherical morph average polar angle maps are projected back to the inflated right and left hemispheres of one subject, and shown in lateral (top), posterior (middle-top), medial (middle-bottom), and inferior (bottom) views. The posterior boundary of ipsilateral visual responses is marked by a thick yellow dashed line. Thin dotted lines indicate the boundaries of regions with high quantitative R_1 values traced from Figure 4. Vertical and horizontal meridians traced from field sign calculations (not shown) are shown as lines of small circles and thick black dashes. Generalized visual and multisensory area names (V1, V2, V3, VP/V3v, V6, V6A, V8/VO1, V3A, MT/V5, FST, LIP (multiple), VIP (multiple), PrCu [pre-cuneus visual area]) were drawn judiciously from the existing conflicting literature.

Figure 4. Cross-subject surface average quantitative R_1 ($=1/T_1$) maps. Spherical morph average maps of quantitative R_1 values sampled at 50% of cortical thickness are projected back to the same subject as in Figure 3, and posed and annotated identically. Quantitative R_1 is illustrated as variation from the mean (ΔR_1) after removing variance due to local cortical curvature. A histogram of ΔR_1 values from 3 right hemisphere visual areas (V6, MT, and VIP, defined by retinotopy) and 2 right hemisphere non-visual areas (inferior pre-cuneus "default mode" area and non-visual lateral occipital cortex) is shown in the lower middle inset. The non-visual regions of interest are shown as dashed lines in matching blue and green (upper left and middle left). The maxima shown are 3–4% higher than the average R_1.

the middle of the oval. This region was located within a sulcus (Supplementary Fig. 2, showing individual subject data on each folded surface; the average was also resampled to each subject and shown as a green outline). We labeled the posterior part MT. To avoid name proliferation, we labeled the anterior and inferior part of this area, fundus of the superior temporal sulcus area (FST), on the basis of a similar retinotopic layout in non-human primates [e.g. macaque monkey, owl monkeys; see also Kolster et al. (2010) and Amano et al. (2009) who have subdivided this region into a larger number of areas with somewhat different names].

In dorsolateral occipital cortex near the midline, we identified a patch of high R_1 ($\Delta R_1 \sim 0.028 \text{ s}^{-1}$) that corresponded well with V3A (defined by the first appearance of upper field here moving anteriorly) in the left hemisphere and roughly so
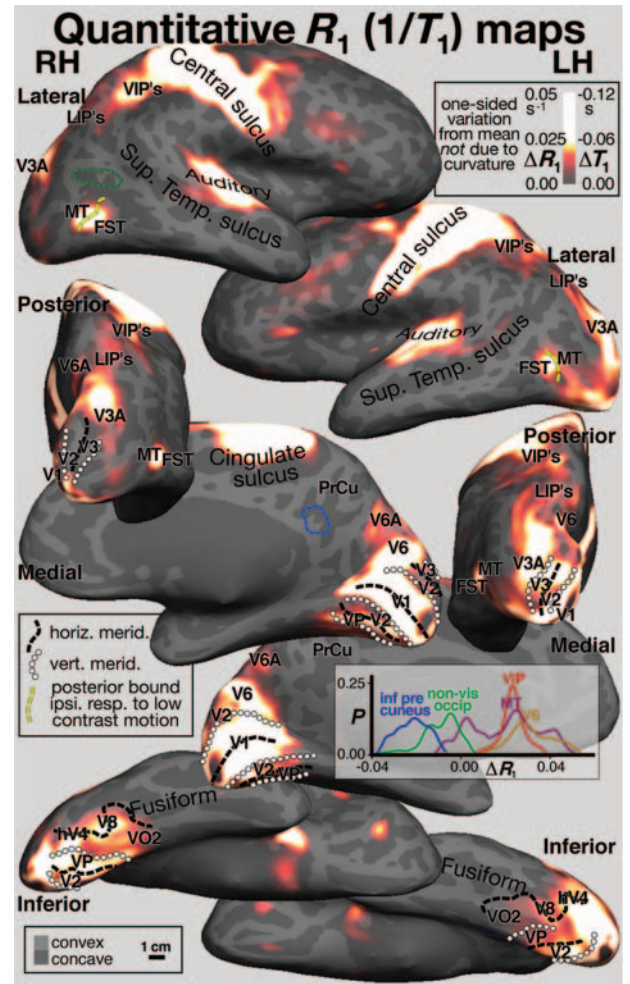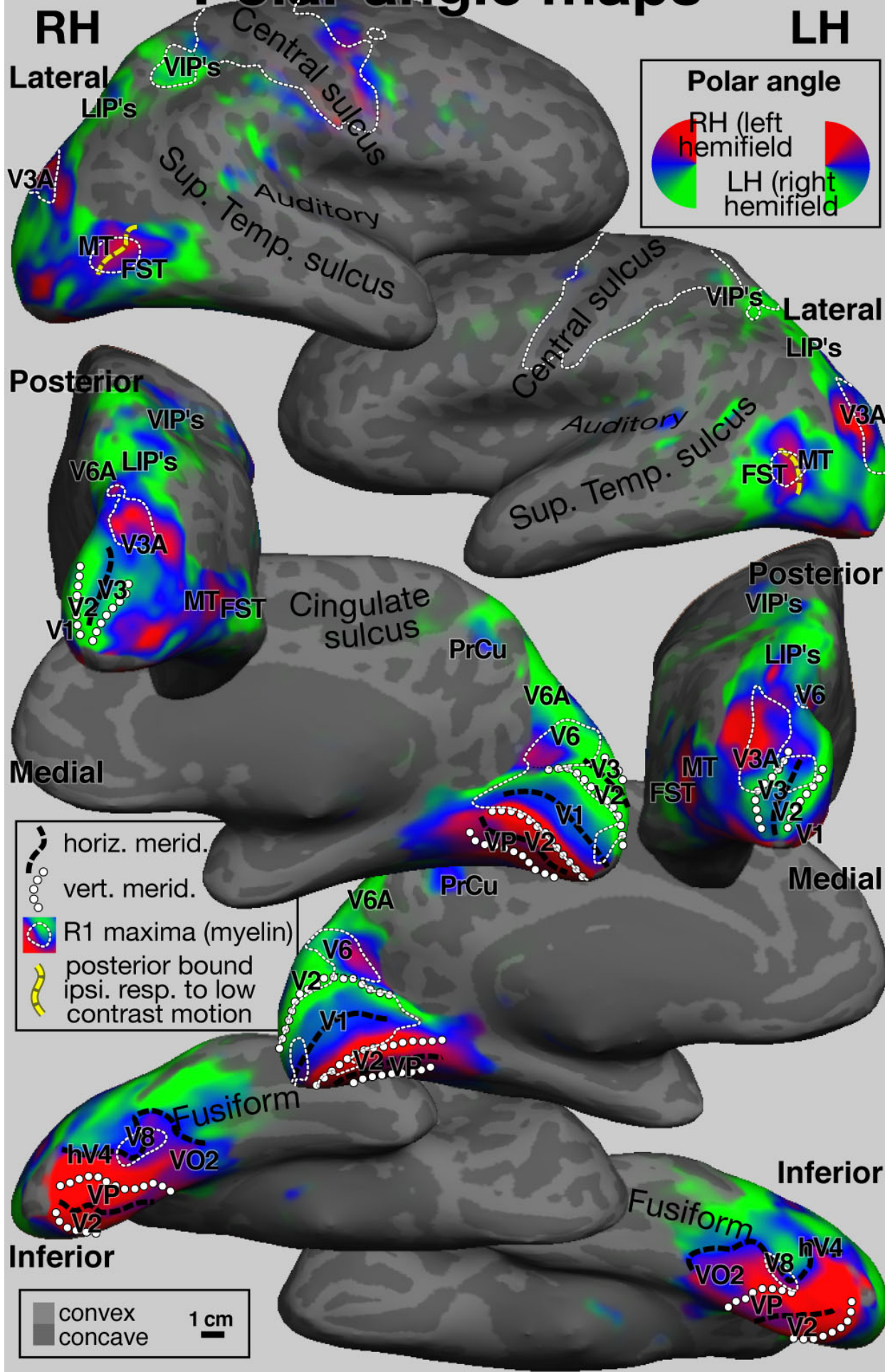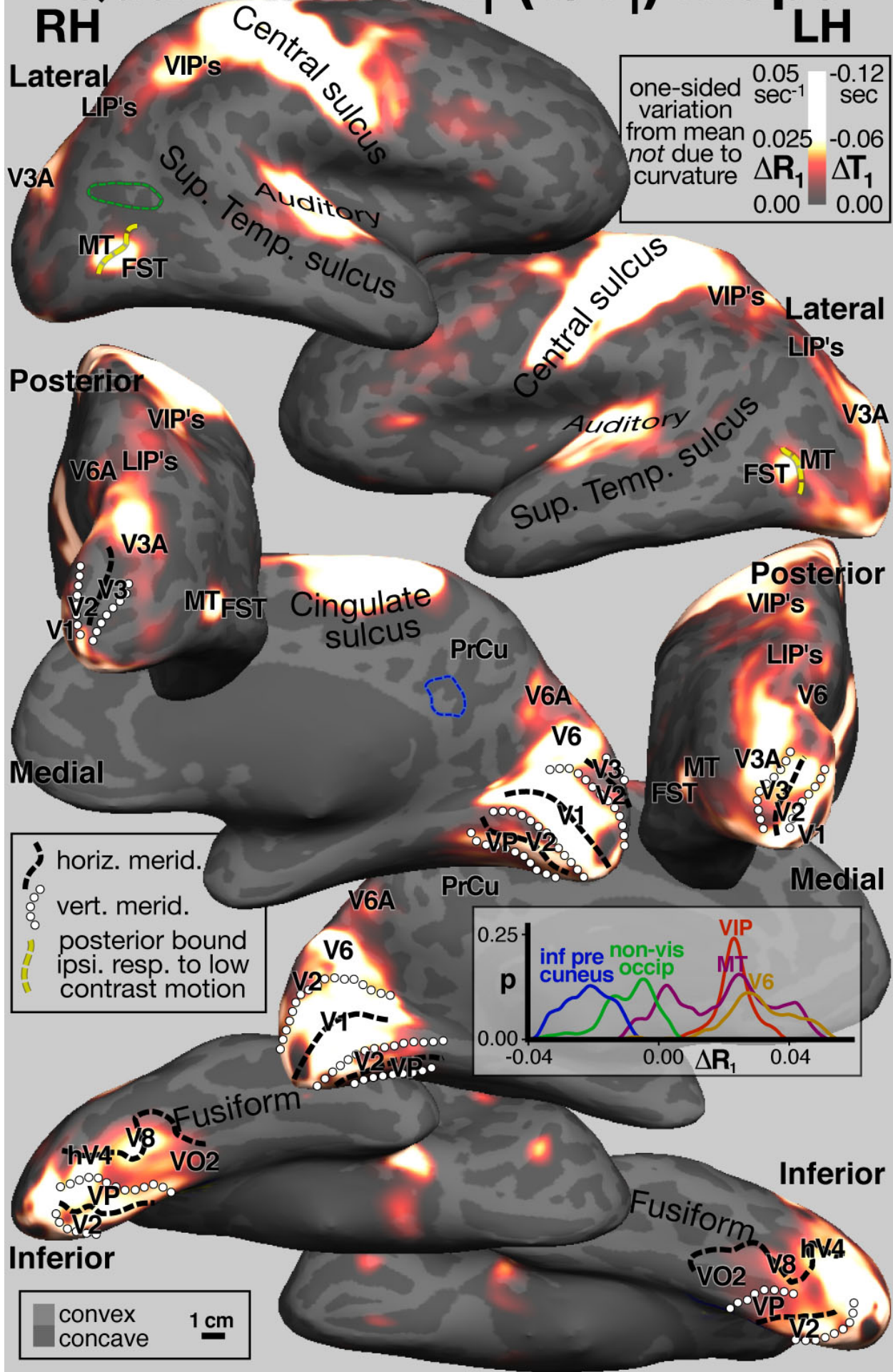
in the right. Inferiorly, beginning with the center-of-gaze representation of V1 (see inferior view), there is a large anteriorly extending region of high R_1 values ($\Delta R_1 \sim 0.031 \text{ s}^{-1}$) that also covers the adjoining center-of-gaze representations V2, V3/VP, and hV4 in both hemispheres. This maximum extends across parts of at least 4 different visual areas and may be artifactual (see Discussion). Still on the inferior surface, moving medially along the horizontal meridian of hV4 (Wandell et al. 2007), an anterior right-angle bend is visible in a region originally identified as V8 by Hadjikhani et al. (1998). This precisely corresponds to a small maximum of R_1 ($\Delta R_1 \sim 0.021 \text{ s}^{-1}$) in both hemispheres.

Back on the lateral surface, there is a prominent maximum of R_1 ($\Delta R_1 \sim 0.020 \text{ s}^{-1}$) in both hemispheres at the expected location of the ventral intraparietal area (VIP) (Sereno and Huang 2006). This is connected to the large high R_1 strip in somatosensory and motor cortex via a small isthmus. In our

Polar angle maps

RH

Lateral
LIP's
VIP's
Central sulcus
V3A
Auditory
MT
Sup. Temp. sulcus
FST

Posterior
VIP's
V6A LIP's
V3A
V3
V2
V1
MT FST
Cingulate sulcus

Polar angle
RH (left hemifield)
LH (right hemifield)

LH
Central sulcus
VIP's
Lateral
LIP's
V3A
Auditory
FST MT
Sup. Temp. sulcus

Posterior
VIP's
LIP's
V6
MT V3A
FST V3
V2
V1

Medial
PrCu
V6A
V6
V3
V2
V1
VP V2
PrCu

horiz. merid.
vert. merid.
R1 maxima (myelin)
posterior bound ipsi. resp. to low contrast motion

V6A
V6
V2
V1
V2 VP
Fusiform
V8
hV4
VO2
VP
V2

Medial

Inferior
Fusiform
VO2 V8 hV4
VP
V2

Inferior

convex
concave
1 cm

Quantitative R_1 ($1/T_1$) maps

RH

Lateral

LIP's

VIP's

Central sulcus

V3A

Auditory

MT

Sup. Temp. sulcus

FST

one-sided
variation
from mean
not due to
curvature

0.05 sec⁻¹   -0.12 sec

0.025   -0.06

ΔR_1 ΔT_1

0.00   0.00

LH

Central sulcus

VIP's

Lateral

LIP's

Auditory

V3A

FST   MT

Sup. Temp. sulcus

Posterior

VIP's

V6A   LIP's

V3A

V3

V2

V1

MT FST   Cingulate sulcus

PrCu

V6A

V6

V3

V2

V1

VP V2

Posterior

VIP's

LIP's

V6

MT   V3A

FST   V3

V2

V1

Medial

horiz. merid.

vert. merid.

posterior bound
ipsi. resp. to low
contrast motion

PrCu

V6A

V6

V2

V1

V2 VP

Medial

0.25

p

inf pre cuneus   non-vis occip   VIP

MT   V6

0.00

-0.04   0.00 ΔR_1 0.04

Fusiform

V8

hV4   VO2

VP

V2

Inferior

Inferior

Fusiform

VO2   V8   hV4

VP

V2

convex
concave

1 cm

polar angle mapping, this region contained lower visual field and horizontal meridian responses. The lower field bias may partly reflect head-centered remapping of receptive fields as a result of the lowered gaze position common with direct-view mapping.

Just posterior to VIP, best visible in the posterior view, there is an elongated region of moderately high R_1 values ($\Delta R_1 \sim 0.013 \text{ s}^{-1}$) in both hemispheres that extends posteriorly through the region originally identified as the human intraparietal area (LIP) (Sereno et al. 2001) eventually joining up with the prominent V3A maximum. Subsequently, this region has been subdivided into a number of LIP's (or IPS's) and contains several somewhat variable visual maps (e.g. Swisher et al. 2007; Silver and Kastner 2009). Finally, in frontal cortex, there are shallow R_1 maxima in the frontal eye fields, in an area identified as the polysensory zone (Graziano and Gandhi 2000; Sereno and Huang 2006; Huang and Sereno 2007), which appears as an extension off the motor strip, and there is a shallow R_1 maximum in the retinotopic part of the dorsolateral prefrontal cortex (Hagler and Sereno 2006).

Discussion

Cortical-surface-based analysis of quantitative longitudinal relaxation rate, R_1 ($=1/T_1$), showed reliable small (1–4%) regional differences in cortical gray matter likely due to differences in myelination, as verified by test–retest and by statistical analysis in selected regions defined in previous studies (postmortem-defined V1 and MT, angular gyrus). We compared this in vivo architectonic measure with retinotopic mapping data obtained in separate sessions from the same subjects. This revealed that a number of boundaries visible in the R_1 maps correspond to previously recognized retinotopic borders, demonstrating the feasibility of using R_1 maps to help with cortical parcellation. Though not all adjoining areas have distinguishable R_1 values, a number can now be identified structurally without elaborate functional scans.

The cortex-wide average of R_1 as a function of laminar depth resembled postmortem myeloarchitectonic measures, systematically decreasing from the gray–white matter border to the pial surface with a moderate plateau in middle layers. These results are consistent with findings from localized high-resolution imaging and postmortem imaging (Walters et al. 2003; Eickhoff et al. 2005). The R_1 ranking of different ROIs—from most to least myelinated—is also remarkably consistent over sampling depths.

R_1 was significantly related to local curvature at intermediate depths—with convex parts of the cortex more strongly myelinated—quantitatively confirming observations in myelin-stained sections (Smart and McSherry 1986; Annese et al. 2004). Local curvature predicted R_1 better than a measure of whether a cortical region was on a sulcus or gyrus (the primary measure used for cross-subject surface alignment; Fischl et al. 1999). The strength and generality of this finding across the cortex suggests that there is a fundamental asymmetry between concave and convex bends in the cortex having to do with differences in the way deeper and more superficial layers can be deformed (Xu et al. 2010).

At a macroscopic level, the pattern of R_1 across the cortex showed a remarkable resemblance to postmortem studies of the order of myelogenesis (Flechsig 1920). By comparing these R_1 maps with retinotopic maps, we found that the borders of a number of visual areas defined in the same subjects—including V1, V3A, V6, V6A, V8, VIP, retinotopic dorsolateral prefrontal cortex, and the frontal eye fields—were marked by abrupt increases in R_1 (0.02–0.04 s^{-1}). Perhaps our most surprising finding concerned the heavily myelinated oval in the lateral occipital cortex. Previously identified as MT/V5 in a number of studies, retinotopic mapping (polar angle, posterior boundary of ipsilateral responses) showed that MT proper only accounted for the posterior 1/3 to 1/2 of that oval. This suggests that previous in vivo and postmortem studies in humans may have overestimated the extent of MT. Given that there are several areas with above average myelination anterior and inferior to MT in monkeys (MST and FST—e.g. Bock et al. 2009), this observation is not unprecedented; however, those other areas may be relatively larger or contain additional subdivisions in humans. Somatomotor and auditory cortex were also prominently recognizable (treated elsewhere).

Potential Applications

In contrast to T_1w imaging, quantitative R_1 imaging directly estimates a basic physical property, the longitudinal relaxation rate of protons in a given tissue. Thus, the resulting maps are directly comparable without intensity normalization across individuals, scanners, and time—which especially lends itself to studying cortical areal differences, development, health versus disease, and disease progression. In this respect, quantitative neuroimaging is superior to standard postmortem myelin stains, which, despite their much higher resolution, are more subject to the uncontrollable vagaries of silver impregnation.

As an example, R_1 values in middle cortical layers for the high-probability MT label differ significantly from immediately adjacent regions, with an average R_1 value of $\sim 0.62 \text{ s}^{-1}$ at a fractional cortical depth 0.5 (Fig. 1B), and an average de-curved ΔR_1 of 0.023 s^{-1}. To investigate whether this highly myelinated region could be identified on a single subject basis, we thresholded each subject's surface-smoothed (4-mm FWHM) de-curved R_1 map at the average ΔR_1 value of 0.023 s^{-1} and searched for a disconnected supra-threshold R_1 patch within a lateral occipital MT+ search space based on previous human studies (Annese et al. 2005). Such patches were identified in all 6 subjects, and in 11 of 12 hemispheres (Supplementary Fig. 1).

Methodological Issues and Prospects

Automated in vivo mapping of architectonics in single subjects requires detecting local changes in R_1 on the order of 1% at a high isotropic resolution of $\sim$800 um, which is made possible by advanced quantitative methods. In particular, we employed high-quality mapping of the B1+ transmit field (Lutti et al. 2010, 2012) and highly sensitive multi-echo 3D FLASH R_1 mapping to achieve maximal resolution, accuracy, and precision in the shortest time possible (Weiskopf et al. 2011). We optimized the TR, flip angle and RF spoiling phase increment for highest accuracy and precision (Helms et al. 2011) and applied corrections for imperfect spoiling of magnetization coherence pathways (Preibisch and Deichmann 2009). No post hoc brightness intensity normalization was used. The excellent scan-rescan reproducibility (Fig. 2) demonstrates that our R_1 estimates are robust, showing that quantitative in vivo maps can be obtained in only 25 min of

scan time (see Supplementary Information for further discussion and description of R_1 mapping).

In recent work done in parallel with ours, cortical myelination has been estimated using a ratio between T_1w and T_2w scans (Glasser and Van Essen 2011). The results were broadly similar to ours but focused on large group results. Also, an additional series of post hoc normalization steps were required to visualize this non-quantitative data, which contain uncorrected artifacts in tissue contrast and brightness due to non-uniform B1$^+$ transmit fields and to the effects of dividing pixel values from the 2 different image types that have contrasts sensitive to different aspects of microanatomy as well as different artifacts. The normalization steps are more difficult to reproduce at other centers than would be a hard threshold at cortical depth = 0.5 of $R_1 = 0.62$ s^{-1}.

Although local increases in cortical R_1 corresponded well with known patterns of myelination and with retinotopically defined areas, there were some unexpected local increases in R_1—for example, at the nearly adjoined center-of-gaze regions of V1, V2, V3, and hV4. Because R_1 differences between cortical areas are comparable with R_1 differences between different cortical depths (Fig. 1), detection of interareal differences requires uniformly accurate estimation of the gray–white and pial surfaces just as much as it requires R_1 uniformity. To improve those estimates, the more uniform R_1 images rather than T_1w images could be used to reconstruct the pial surface. However, this will require extending the current FreeSurfer pial-surface-finding algorithm, which is finely adapted to T_1w image intensity relations among tissue types. For example, in quantitative R_1 images, there is no change in image intensity between the superior margin of the cerebellum and inferior margin of the inferior occipital lobe—which leads to a ballooning of the pial surface there—whereas in T_1w images, the cerebellum and inferior occipital lobe are separated by a thin but distinct hypointensity corresponding to the dura—likely a mixed contrast artifact, but one that FreeSurfer relies on. Another region where the FreeSurfer pial-surface reconstruction using R_1 images fails is near the thin temporal bone. It will be necessary to strategically incorporate quantitative proton density images into the pipeline to resolve this surface-reconstruction problem.

Another problem arises in areas such as S-I and V1 where parts of the cortical ribbon are so thin (~1.5 mm) that they are spanned by less than two 0.8 mm^3 voxels. The problem of misestimating the cortical depth fraction and hence misestimating R_1 is particularly acute in this case, which might explain the unexpected reduction in R_1 in parafoveal V1 (see medial surface views in Fig. 3).

Quantitative R_1 mapping is fitted to answering a number of questions beyond those introduced here. For example, we are currently using it to characterize auditory and somatomotor fields (Dick et al. 2011) and are combining it with high-angular-resolution diffusion measurements in the cortex. This method could also illuminate structure/function mapping within cortical areas (e.g. in V2 stripes). Finally, the significant individual differences in local quantitative R_1 we have uncovered may have functional correlates.

Supplementary Material

Supplementary material can be found at: http://www.cercor.oxfordjournals.org/.

Notes

All authors participated in data collection, data analysis, and preparation of this paper. *Conflict of Interest*: None declared.

References

Allman JM, Kaas JH. 1971. A representation of the visual field in the caudal third of the middle temporal gyrus of the owl monkey (Aotus trivirgatus). Brain Res. 31:85–105.

Amano K, Wandell BA, Dumoulin SO. 2009. Visual field maps, population receptive field sizes, and visual field coverage in the human MT+ complex. J Neurophysiol. 102:2704–2718.

Annese J, Gazzaniga MS, Toga AW. 2005. Localization of the human cortical visual area MT based on computer aided histological analysis. Cereb Cortex. 15:1044–1053.

Annese J, Pitiot A, Dinov ID, Toga AW. 2004. A myelo-architectonic method for the structural classification of cortical areas. Neuroimage. 21:15–26.

Bailey P, von Bonin G. 1951. The isocortex of man. Urbana: University of Illinois Press.

Bock NA, Kocharyan A, Liu JV, Silva AC. 2009. Visualizing the entire cortical myelination pattern in marmosets with magnetic resonance imaging. J Neurosci Meth. 185:15–22.

Braak H. 1980. Architectonics of the human telencephalic cortex. New York: Springer-Verlag.

Caspers S, Schleicher A, Bacha-Trams M, Palomero-Gallagher N, Amunts K, Zilles K. 2012. Organization of the human inferior parietal lobule based on receptor architectonics. Cereb Cortex. doi:10.1093/cercor/bhs048.

Clark VP, Courchesne E, Grafe M. 1992. In vivo myeloarchitectonic analysis of human striate and extrastriate cortex using magnetic resonance imaging. Cereb Cortex. 2:417–424.

Dale AM, Fischl B, Sereno MI. 1999. Cortical surface-based analysis. I. Segmentation and surface reconstruction. Neuroimage. 9:179–194.

DeYoe EA, Carman G, Bandettini P, Glickman S, Cox R, Miller D, Neitz J. 1996. Mapping striate and extrastriate visual areas in human cerebral cortex. Proc Natl Acad Sci USA. 93:2382–2386.

Dick F, Tierney AT, Weiskopf N, Lutti A, Sereno MI. 2011. Combined tonotopic and myeloarchitectonic mapping of human auditory regions. In: Neuroscience meeting planner. Washington (DC). Program No. 171.26.

Draganski B, Ashburner J, Hutton C, Kherif F, Frackowiak RSJ, Helms G, Weiskopf N. 2011. Regional specificity of MRI contrast parameter changes in normal ageing revealed by voxel-based quantification (VBQ). Neuroimage. 55:1423–1434.

Eickhoff S, Walters NB, Schleicher A, Kril J, Egan GF, Zilles K, Watson JDG, Amunts K. 2005. High-resolution MRI reflects myeloarchitecture and cytoarchitecture of human cerebral cortex. Hum Brain Mapp. 24:206–215.

Engel SA, Rumelhart DE, Wandell BA, Lee AT, Glover GH, Chichilnisky EJ, Shadlen MN. 1994. fMRI of human visual cortex. Nature. 36:525.

Fischl B, Dale AM. 2000. Measuring the thickness of the human cerebral cortex from magnetic resonance images. Proc Natl Acad Sci USA. 97:11050–11055.

Fischl B, Rajendran N, Busa E, Augustinack J, Hinds O, Yeo BTT, Mohlberg H, Amunts K, Zilles K. 2008. Cortical folding patterns and predicting cytoarchitecture. Cereb Cortex. 18:1973–1980.

Fischl B, Sereno MI, Tootell RB, Dale AM. 1999. High-resolution inter-subject averaging and a coordinate system for the cortical surface. Hum Brain Mapp. 8:272–284.

Flechsig P. 1920. Antomie des menschlichen Gehirns und Rückenmarks auf myelogenetischer Grundlage. Leipzig: Georg Thieme.

Gamberini M, Galletti C, Bosco A, Breveglieri R, Fattori P. 2011. Is the medial posterior parietal area V6A a single functional area? J Neurosci. 31:5145–5157.

Geyer S, Weiss M, Reimann K, Lohmann G, Turner R. 2011. Microstructural parcellation of the human cerebral cortex – from Brodmann's post-mortem map to in vivo mapping with high-field magnetic resonance imaging. Front Hum Neurosci. 5. doi: 10.3389/fnhum.2011.00019.

Glasser MF, Van Essen DC. 2011. Mapping human cortical areas in vivo based on myelin content as revealed by t1- and t2-weighted MRI. J Neurosci. 31:11597–11616.

Graziano MS, Gandhi S. 2000. Location of the polysensory zone in the precentral gyrus of anesthetized monkeys. Exp Brain Res. 135:259–266.

Hadjikhani N, Liu AK, Dale AM, Cavanagh P, Tootell RB. 1998. Retinotopy and color sensitivity in human visual cortical area V8. Nat Neurosci. 1:235–241.

Hagler DJ, Riecke L, Sereno MI. 2007. Parietal and superior frontal visuospatial maps activated by pointing and saccades. Neuroimage. 35:1562–1577.

Hagler DJ, Sereno MI. 2006. Spatial maps in frontal and prefrontal cortex. Neuroimage. 29:567–577.

Helms G, Dathe H, Dechent P. 2008. Quantitative FLASH MRI at 3T using a rational approximation of the Ernst equation. Magn Reson Med. 59:667–672.

Helms G, Dathe H, Weiskopf N, Dechent P. 2011. Identification of signal bias in the variable flip angle method by linear display of the algebraic Ernst equation. Magn Reson Med. 66:669–677.

Helms G, Draganski B, Frackowiak R, Ashburner J, Weiskopf N. 2009. Improved segmentation of deep brain grey matter structures using magnetization transfer (MT) parameter maps. Neuroimage. 47:194–198.

Helms G, Finsterbusch J, Weiskopf N, Dechent P. 2008. Rapid radiofrequency field mapping in vivo using single-shot STEAM MRI. Magn Reson Med. 60:739–743.

Huang R-S, Sereno MI. 2007. Dodecapus: an MR-compatible system for somatosensory stimulation. Neuroimage. 34:1060–1073.

Huk AC, Dougherty RF, Heeger DJ. 2002. Retinotopy and functional subdivision of human areas MT and MST. J Neurosci. 22:7195–7205.

Kolster H, Peeters R, Orban GA. 2010. The retinotopic organization of the human middle temporal area MT/V5 and its cortical neighbors. J Neurosci. 30:9801–9820.

Lashley KS, Clark G. 1946. The cytoarchitecture of the cerebral cortex of Ateles; a critical examination of architectonic studies. J Comp Neurol. 85:223–305.

Lutti A, Hutton C, Finsterbusch J, Helms G, Weiskopf N. 2010. Optimization and validation of methods for mapping of the radiofrequency transmit field at 3T. Magn Reson Med. 64:229–238.

Lutti A, Stadler J, Josephs O, Windischberger C, Speck O, Bernarding J, Hutton C, Weiskopf N. 2012. Robust and fast whole brain mapping of the RF transmit field B1 at 7T. PLoS One. 7:e32379. doi:10.1371/journal.pone.0032379.

Malikovic A, Amunts K, Schleicher A, Mohlberg H, Eickhoff SB, Wilms M, Palomero-Gallagher N, Armstrong E, Zilles K. 2007. Cytoarchitectonic analysis of the human extrastriate cortex in the region of V5/MT+: a probabilistic, stereotaxic map of area hOc5. Cereb Cortex. 17:562–574.

Merzenich MM, Kaas JH. 1980. Principles of organization of sensory-perceptual systems in mammals. Prog Psychobiol Physiol Psych. 9:1–42.

Meynert T. 1867. Der Bau der Grosshirnrinde und seine örtlichen Verschiedenheiten nebst einem pathologisch-anatomischen Corollarium. Vjschr Psychiat. 1:198–217.

Pitzalis S, Galletti C, Huang R-S, Patria F, Committeri G, Galati G, Fattori P, Sereno MI. 2006. Wide-field retinotopy defines human cortical visual area V6. J Neurosci. 26:7962–7973.

Preibisch C, Deichmann R. 2009. Influence of RF spoiling on the stability and accuracy of T_1 mapping based on spoiled FLASH with varying flip angles. Magn Reson Med. 61:125–135.

Schmierer K, Scaravilli F, Altmann DR, Barker GJ, Miller DH. 2004. Magnetization transfer ratio and myelin in postmortem multiple sclerosis brain. Ann Neurol. 56:407–415.

Sereno MI, Dale AM, Reppas JB, Kwong KK, Belliveau JW, Brady TJ, Rosen BR, Tootell RB. 1995. Borders of multiple visual areas in humans revealed by functional magnetic resonance imaging. Science. 268:889–893.

Sereno MI, Huang R-S. 2006. A human parietal face area contains aligned head-centered visual and tactile maps. Nat Neurosci. 9:1337–1343.

Sereno MI, Pitzalis S, Martinez A. 2001. Mapping of contralateral space in retinotopic coordinates by a parietal cortical area in humans. Science. 294:1350–1354.

Sigalovsky IS, Fischl B, Melcher JR. 2006. Mapping an intrinsic MR property of gray matter in auditory cortex of living humans: a possible marker for primary cortex and hemispheric differences. Neuroimage. 32:1524–1537.

Silver MA, Kastner S. 2009. Topographic maps in human frontal and parietal cortex. Trends Cogn Sci. 13:488–495.

Smart IH, McSherry GM. 1986. Gyrus formation in the cerebral cortex of the ferret. II. Description of the internal histological changes. J Anat. 147:27–43.

Swisher JD, Halko MA, Merabet LB, McMains SA, Somers DC. 2007. Visual topography of human intraparietal sulcus. J Neurosci. 27:5326–5337.

Walters NB, Egan GF, Kril JJ, Kean M, Waley P, Jenkinson M, Watson JDG. 2003. In vivo identification of human cortical areas using high-resolution MRI: an approach to cerebral structure-function correlation. Proc Natl Acad Sci USA. 100:2981–2986.

Wandell BA, Dumoulin SO, Brewer AA. 2007. Visual field maps in human cortex. Neuron. 56:366–383.

Weiskopf N, Lutti A, Helms G, Novak M, Ashburner J, Hutton C. 2011. Unified segmentation based correction of R1 brain maps for RF transmit field inhomogeneities (UNICORT). Neuroimage. 54:2116–2124.

Xu G, Knutsen AK, Dikranian K, Kroenke CD, Bayly PV, Taber LA. 2010. Axons pull on the brain, but tension does not drive cortical folding. J Biomech Eng. 132:071013–1–071013–8.

Zilles K, Amunts K. 2010. Centenary of Brodmann's map–conception and fate. Nat Rev Neurosci. 11:139–145.

Supplementary Information Inventory

1. Functional imaging -- additional details on scanner pulse sequences and visual stimuli
2. Analysis of regional differences in R_1 -- details of R_1 ROI analysis
3. Functional analyses -- details of analysis of functional MRI data
4. References -- cited in supplemental text
5. Supplemental figure captions
6. Supplemental movie caption -- attached to main Figure 4, animated viewpoint, contrast changes

1. Functional imaging: Functional images were acquired on a 1.5 whole-body Tim Avanto System (Siemens Healthcare), at the Birkbeck/UCL Centre for NeuroImaging, with body transmit and 32-channel receive head coil. EPI images were acquired with the following parameters: 24 slices, voxel resolution 3.2 x 3.2 x 3.2 mm^3 (matrix size: 64 x 64), flip angle = 90°, bandwidth = 1474 Hz/pixel, TR = 2000ms, TE = 39ms, data acquired with prospective motion correction (Thesen et al., 2000). Individual polar angle and eccentricity scans had 260 volumes; individual ipsilateral mapping scans had 132 volumes. To allow longitudinal relaxation to come to equilibrium, 6 initial volumes were discarded from each run (2 initial not saved by scanner). For each imaging session, a short (3 min) T_1-weighted 3D MPRAGE (88 partitions, voxel resolution 1 x 1 x 2 mm^3, flip angle = 7°, TE = 4 ms, TI = 1000 ms, TR = 8.2 ms, mSENSE accel. = 2x, slab-selective excitation) was acquired with the same orientation and slice block center as the functional data for initial alignment with the high-resolution scans used to reconstruct the subject's cortical surface. Five of six subjects completed at least 8 retinotopy scans (4 scans in one subject) and 4 ipsilateral mapping scans (2560 volumes per subject) across 3 to 5 additional sessions.

In-house OpenGL/Xlib stimulus presentation software running on Mac OS X and Linux was used to generate visual stimuli that were projected into the bore using an Eiki LC-XG300 XGA video projector onto a translucent direct-view screen at the participant's upper chest level. The visual field was stimulated to an eccentricity of at least 57 degrees of visual angle in all directions from the central fixation dot to avoid artifacts due to 'off-the-edge' inhibition. A black matte shroud situated just outside the bore blocked the beam from making low-angle reflections off the top of the bore. The rear of the head coil was elevated with a wooden wedge to help tilt the head forward. Subjects' fixation and general attention was monitored using a custom-built in-bore camera (Oliver Josephs). Responses were made via an optical-to-USB response box (LUMItouch, Photon Control, Burnaby, Canada) situated under their right hand.

For polar angle and eccentricity mapping, a continuously rotating wedge or expanding/contracting ring (all with eight 64 sec cycles) was populated with a random-colored checkerboard with 50% luminance contrast, expanding, contracting and dilating dot fields, and two simultaneous streams of objects (black-and-white faces and letters) at random positions. The stimuli were designed to evoke simultaneous activation in the maximum number of lower- and higher-level visual fields including V6 (Pitzalis et al., 2010). To maintain high levels of peripheral attention during central fixation, subjects pressed a button when they saw either an occasional number (in the letters stream) or an occasional upside-down face (in the right-side-up faces stream) within the ring or wedge. Runs alternated between counter-clockwise and clockwise, and expanding and contracting. Stimuli for low contrast ipsilateral field mapping were unilateral light-gray concentric rings presented on gray

background (<5% luminance contrast), masked to an eccentricity of 8 degrees and a polar angle of 22.5 degrees away from the upper and lower visual field vertical meridians. During the 16-second ON blocks, the rings flowed in and out to avoid after-effects, alternating direction every second; in OFF blocks, the rings were static. Runs alternated between left and right hemifield, and starting ON versus starting OFF.

2. Analysis of regional differences in R_1: 5 ROIs with large expected myelination differences were defined. First, we used the FreeSurfer V1 label, V1-fs, (Fischl et al., 2008; Hinds et al., 2009). Second, we subdivided the FreeSurfer left and right hemisphere area MT labels (based on post-mortem group anatomical analyses (Malikovic et al., 2007)) into two smoothed (4 mm surface FWHM kernel), non-overlapping MT-high ($0.25 < p < 0.6$) and MT-low ($0.1 < p < 0.25$) ROIs for each subject in each hemisphere. Annese et al. (Annese et al., 2005) compared MT and a portion of the angular gyrus and demonstrated that some parts of the angular gyrus are particularly lightly myelinated. So, finally, we defined two angular gyrus labels: a smaller one, angular (a non-visually responsive region superior to MT based on their anatomical description drawn on individual subjects' left and right hemispheres and spherically morphed (Fischl et al., 1999) to other subjects), and a larger one, angular-fs, from the FreeSurfer parcellation (Destrieux et al., 2010).

Average R_1 within each of the 5 masks for each subject were compared by matched-paired t-tests (one-tailed $p<0.05$, uncorrected) based on these predictions: (1) R_1 in V1 and the two MT ROIs should exceed R_1 in both angular gyrus ROIs at all cortical depths, and that V1 should have the highest R_1, (2) R_1 in high-probability MT should exceed R_1 in surrounding lower probability MT in deeper cortical layers (depth fractions 0.1-0.6).

3. Functional analyses: Functional images were motion-corrected (AFNI 3dvolreg, heptic interpolation), hand-registered (4x4 affine) using initial registration estimate from the 'align' T_1 scan (same block center, slice plane direction as EPI scans), then finely adjusted by manual blink comparison (with contrast-reversed EPI images) to achieve a more exact overlay. Mapping data were analyzed using Fourier methods with individual and group analysis methods as previously described (Sereno et al., 1995; Sereno and Huang, 2006; Saygin and Sereno, 2008). For each scan type, we combined opposite phase stimuli to cancel fixed local differences in hemodynamic delays.

4. References

Annese, J., Gazzaniga, M. S., and Toga, A. W. (2005). Localization of the human cortical visual area MT based on computer aided histological analysis. Cereb Cortex *15*, 1044–1053.

Destrieux, C., Fischl, B., and Dale, A. (2010). ScienceDirect - NeuroImage : Automatic parcellation of human cortical gyri and sulci using standard anatomical nomenclature. NeuroImage.

Fischl, B., Rajendran, N., Busa, E., Augustinack, J., Hinds, O., Yeo, B. T. T., Mohlberg, H., Amunts, K., and Zilles, K. (2008). Cortical folding patterns and predicting cytoarchitecture. Cerebral Cortex *18*, 1973–1980.

Fischl, B., Sereno, M. I., Tootell, R. B., and Dale, A. M. (1999). High-resolution intersubject averaging and a coordinate system for the cortical surface. Hum Brain Mapp *8*, 272–284.

Hinds, O., Polimeni, J. R., Rajendran, N., Balasubramanian, M., Amunts, K., Zilles, K., Schwartz, E. L., Fischl, B., and Triantafyllou, C. (2009). Locating the functional and anatomical boundaries of human primary visual cortex. NeuroImage *46*, 915–922.

Malikovic, A., Amunts, K., Schleicher, A., Mohlberg, H., Eickhoff, S. B., Wilms, M., Palomero-Gallagher, N., Armstrong, E., and Zilles, K. (2007). Cytoarchitectonic analysis of the human extrastriate cortex in the region of V5/MT+: a probabilistic, stereotaxic map of area hOc5. Cereb Cortex *17*, 562–574.

Pitzalis, S., Sereno, M. I., Committeri, G., Fattori, P., Galati, G., Patria, F., and Galletti, C. (2010). Human v6: the medial motion area. Cereb Cortex *20*, 411–424.

Saygin, A. P., and Sereno, M. I. (2008). Retinotopy and attention in human occipital, temporal, parietal, and frontal cortex. Cereb Cortex *18*, 2158–2168.

Sereno, M. I., Dale, A. M., Reppas, J. B., Kwong, K. K., Belliveau, J. W., Brady, T. J., Rosen, B. R., and Tootell, R. B. (1995). Borders of multiple visual areas in humans revealed by functional magnetic resonance imaging. Science *268*, 889–893.

Sereno, M. I., and Huang, R.-S. (2006). A human parietal face area contains aligned head-centered visual and tactile maps. Nat Neurosci *9*, 1337–1343.

Thesen, S., Heid, O., Mueller, E., and Schad, L. R. (2000). Prospective acquisition correction for head motion with image-based tracking for real-time fMRI. Magn Reson Med *44*, 457–465.

5. Supplemental Figure Captions

Figure S1: In the top panel, individual-subject average relaxation rate (R_1) maps were sampled at cortical depth fraction 0.5, without intensity normalization, and thresholded at $\Delta R_1 = 0.040$ (orange-to-white transition). The main features of the average map in Figure 2 are visible in each subject. Iso-R_1 contours in this data were traced for the inset in Figure 2. The bottom panel shows the same data, posed identically, thresholded for all subjects (also no intensity normalization) at a more liberal $\Delta R_1 = 0.025$.

Figure S2: Individual-subject relaxation rate (R_1) maps on the folded surface (same data as Figure S1, all at same threshold, no intensity normalization). The lateral occipital oval of high R_1 was located in a lateral occipital sulcus in each case. For reference, the surface-based cross-subject average was resampled back to each individual subject's surface (which explains its different shape in each case) via morphed spherical coordinates and outlined in green.

6. Supplemental Movie Caption

Movie S1: The right hemisphere cross-subject surface-averaged R_1 map, sampled back onto an individual subject, is rotated around an oblique axis while the contrast of the color scale (see scale bar at lower right) is repeatedly ramped to better visualize the internal structure of R_1 maxima discussed in the text. The shallow but distinct minima between V1 and V6 (at the superior end of the unfolded parieto-occipital sulcus on the medial occipital lobe surface) and between somatomotor cortex and VIP (in anterior superior parietal cortex) are made more clearly visible.
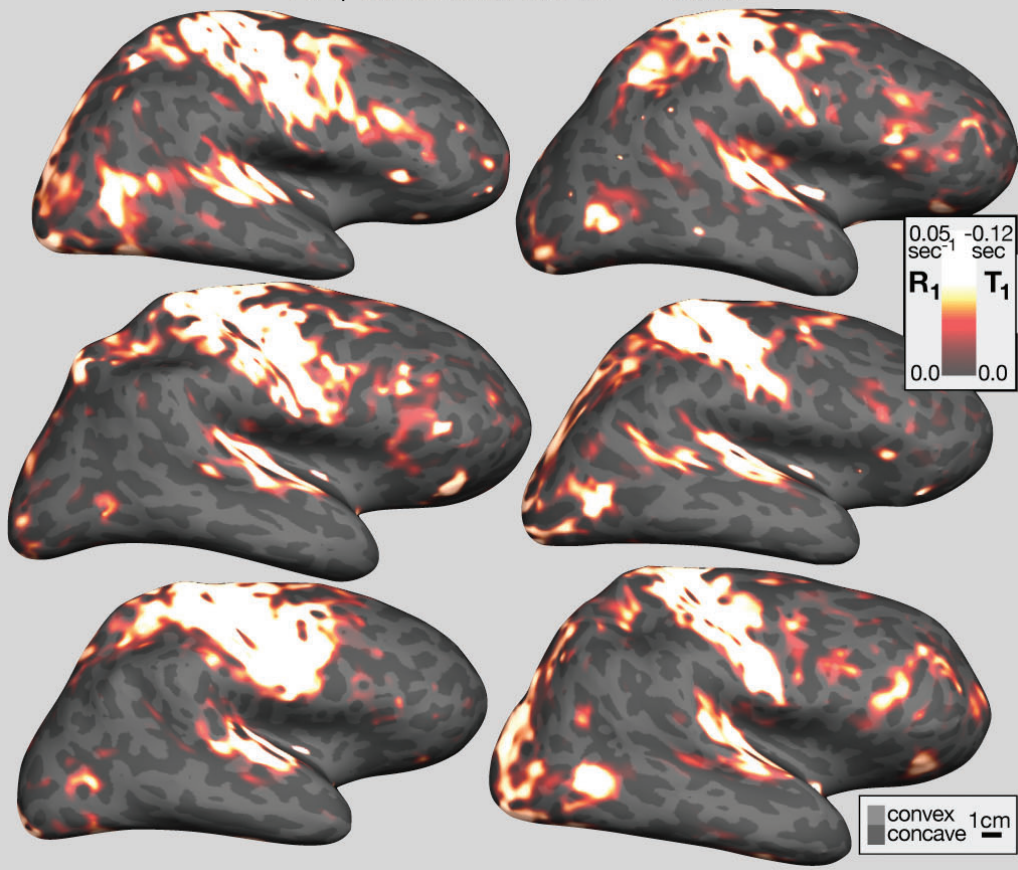
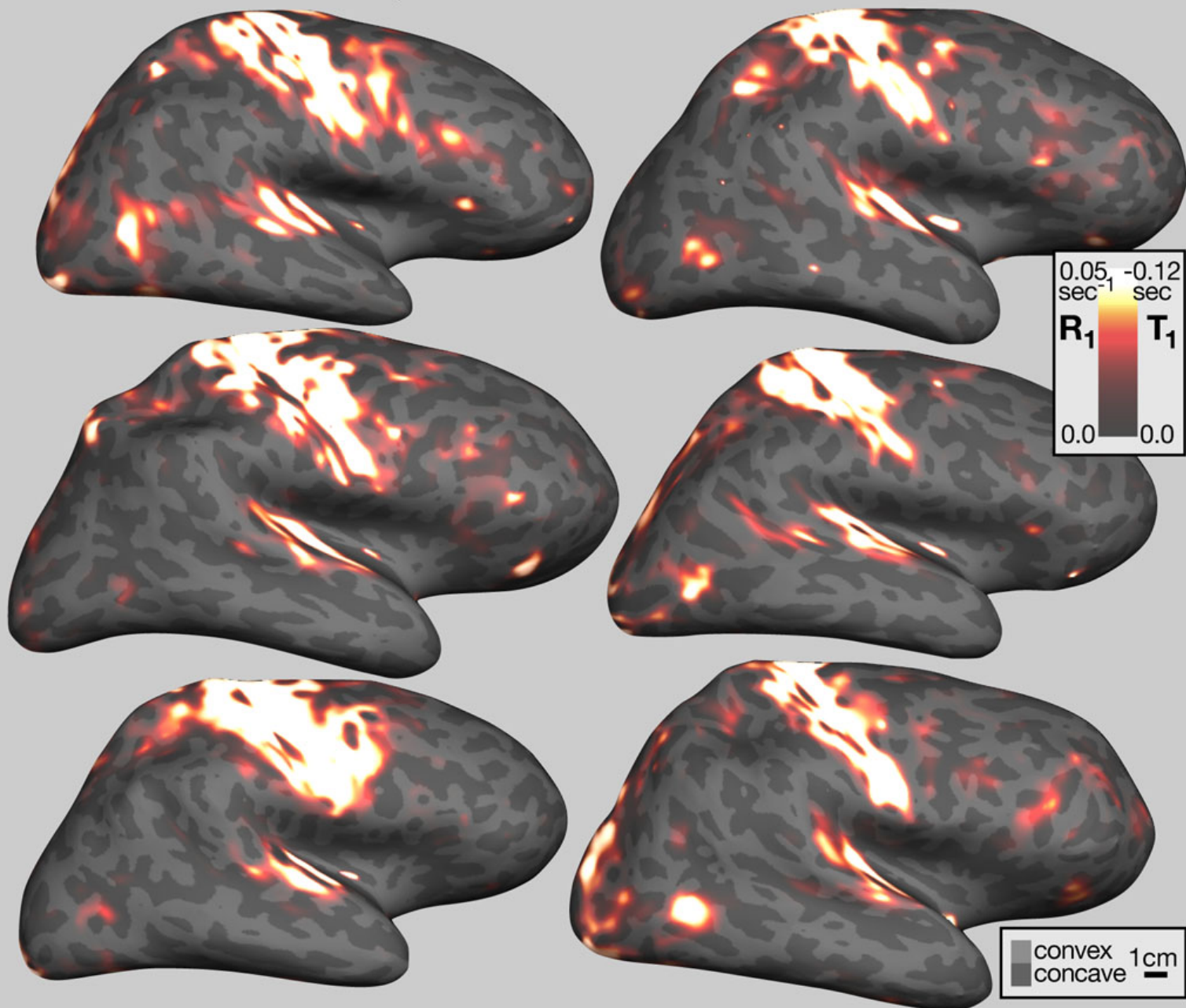**'De-curved' qT1 maps for all participants**

ΔR₁ threshold: 0.040
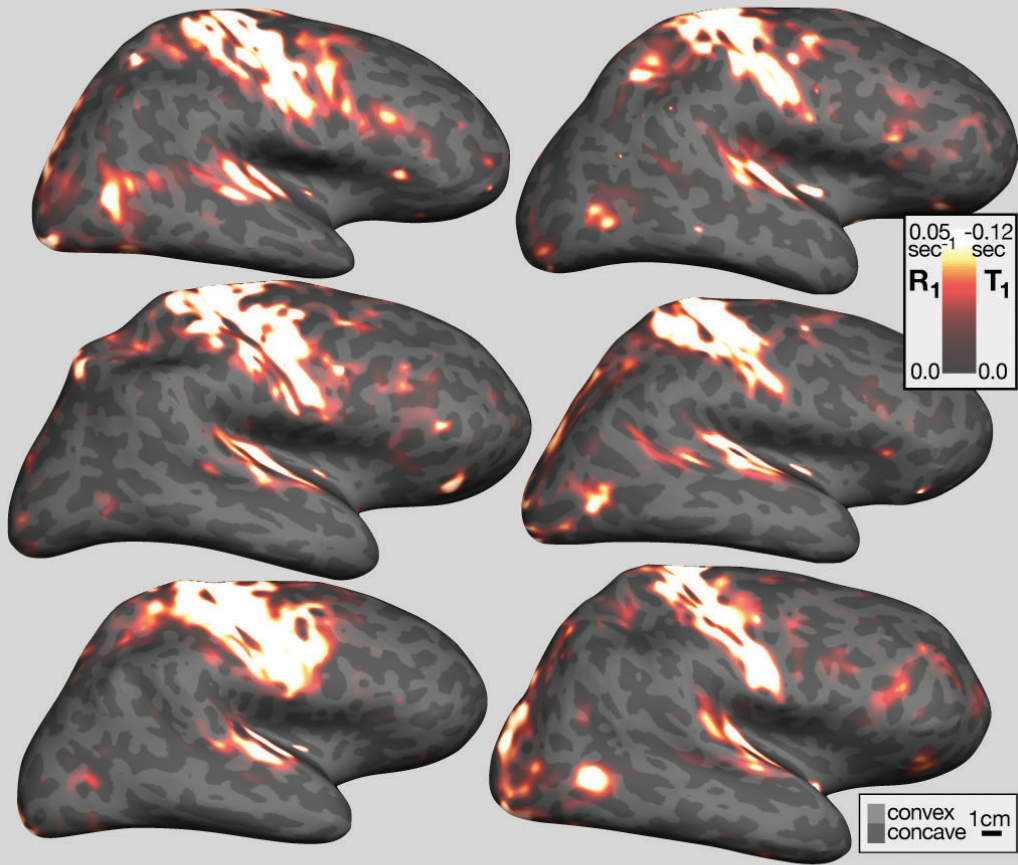
'De-curved' qT1 maps for all participants

ΔR₁ threshold: 0.040 → 0.025

'De-curved' qT1 maps for all participants

ΔR_1 threshold: 0.040

'De-curved' qT1 maps for all participants
ΔR_1 threshold: $0.040 \rightarrow 0.025$

0.05 sec^{-1} -0.12 sec

R$_1$ T$_1$

0.0   0.0

convex
concave   1cm